



**Effect of adaptation functions and multilayer topology on synchronization**Dhrubajyoti Biswas <sup>\*</sup>*Department of Physics, Indian Institute of Technology Madras, Madras 600036, India*Sayan Gupta <sup>†</sup>*The Uncertainty Lab, Department of Applied Mechanics & Biomedical Engineering,  
Indian Institute of Technology Madras, Madras 600036, India  
and Complex Systems and Dynamics Group, Indian Institute of Technology Madras, Madras 600036, India* (Received 19 September 2023; revised 25 January 2024; accepted 31 January 2024; published 27 February 2024)

This study investigates the synchronization of globally coupled Kuramoto oscillators in monolayer and multilayer configurations. The interactions are taken to be pairwise, whose strength adapts with the instantaneous synchronization order parameter. The route to synchronization is analytically investigated using the Ott-Antonsen ansatz for two broad classes of adaptation functions that capture a wide range of transition scenarios. The formulation is subsequently extended to adaptively coupled multilayer configurations, using which a wider range of transition scenarios is uncovered for a bilayer model with cross-adaptive interlayer interactions.

DOI: [10.1103/PhysRevE.109.024221](https://doi.org/10.1103/PhysRevE.109.024221)**I. INTRODUCTION**

Synchronization is an emergent phenomenon observed in coupled dynamical systems [1,2] and has gained significant attention recently. In its most general form, synchronization can be described by constraint relations between the various dynamical variables of a system [3]. This phenomenon can be attributed to the couplings between the individual dynamical units and generally manifests as near-identical dynamics of each constituent unit of the system under specific parametric conditions. It has been observed in a wide spectrum of physical systems such as neuron networks [4,5], electromechanical systems [6–8], fluid dynamics [9–11], and optical systems [12,13] and in different engineering applications [14,15].

Synchronization has been widely studied using the Kuramoto model of phase oscillators [16,17], along with its many variants. This is not only due to its simplicity and analytical tractability but also due to its wide applicability across a host of physical systems, with examples ranging from brain dynamics [18–20], power to grids [21–23], and various others [24–28]. Signatures of synchronization are investigated using order parameters that collectively define the global dynamics of the system and that undergo qualitative changes with reference to one or more parameters. The routes to synchronization provide interesting insights into the dynamical behavior of the system and can be classified into two broad types: continuous and explosive. A continuous transition is characterized by a gradual increase in synchronous behavior when a control parameter is increased beyond a critical value. Explosive transitions, on the other hand, are characterized by discrete jumps, where the system transitions from an asynchronous state to a

synchronous state or vice versa, usually accompanied by hysteresis. Apart from synchronization, explosive transitions can also be observed in the context of other emergent phenomena [29,30].

While the original Kuramoto model considers constant homogenous coupling across different pairs of oscillators, there has been many studies where researchers have considered more complex cases. These include multiplexing [31], incorporating inertia [32], introducing correlations between frequency and coupling strength [33], and integrating time delays into the governing equation [34] among many others [35–40]. Studies [41–44] exist where the strength of the interactions has been taken to be dependent on the instantaneous global state of the system and is referred to as adaptive coupling. This is a common feature in modeling many real-life systems, especially those involving multiphysics interactions. Adaptation is particularly prevalent in biological evolution [45,46], which enables organisms to adjust to new environments. An example that utilizes adaptive coupling could be a model of the political inclination of a group of individuals in a social network. It is expected that the political views of an individual would adapt to the prevailing political climate, which is quantified by the order parameter of the system. However, individuals who were previously aligned may shy away if the global behavior becomes more extreme, due to a certain level of synchrony. This is analogous to the coupling strength being dependent on the synchronization order parameter, potentially in a *nonlinear* and *nonmonotonic* manner. The present study is motivated by this type of problem, where we consider a variant of the Kuramoto model due to its simplicity, analytical tractability, and wide applicability as mentioned earlier.

The rest of the article is arranged as follows: Sec. II discusses the mathematical model of globally coupled Kuramoto oscillators whose interactions are pairwise and adapt to the synchronization order parameter. In Sec. II A analytical

\*dhrubajyoti98@physics.iitm.ac.in

†Corresponding author: sayan@iitm.ac.in

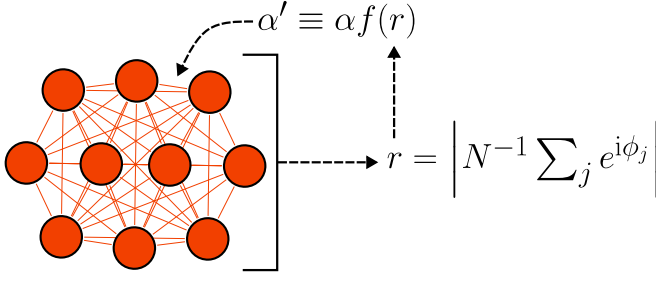


FIG. 1. Schematic of a monolayer phase oscillator system with adaptation.  $\alpha'$  and  $\alpha$  denote the adaptive and nonadaptive coupling strength, respectively.

arguments to determine the transition types are presented. As an example, two broad classes of adaptation functions that encapsulate a wide range of adaptation characteristics are considered in Sec. II B and Sec. II C, respectively. Subsequently, this formulation is extended in Sec. III to the more general case of multilayer networks, with the interactions between the layers being adaptive. The specific example of “cross”-adaptation (discussed later) in a bilayer system is considered in Sec. III A. Section III A 1 presents the cases where the transitions are either explosive or continuous. The more interesting cases involving two different tiered transitions are presented in Sec. III A 2. The paper ends with concluding remarks in Sec. IV.

## II. MONOLAYER CONFIGURATION

The governing equation of an adaptively coupled Kuramoto phase oscillator system is given by [47–49]

$$\frac{d\phi_i}{dt} = \omega_i + \frac{\alpha f(r(t))}{\langle k \rangle} \sum_{j=1}^N A_{ij} \sin(\phi_j - \phi_i), \quad (1)$$

where  $\phi_i \in [0, 2\pi)$  and  $\omega_i \in (-\infty, \infty)$  represent the phase and natural frequency of the  $i$ th oscillator,  $\langle k \rangle$  is the average degree of the underlying network described by the adjacency matrix  $A_{ij}$ , and  $i = 1, 2, \dots, N$ , where  $N$  is the number of oscillators in the system. Generally, the natural frequencies are nonidentical (i.e.,  $\omega_i \neq \omega_j$ ) and are drawn from a distribution  $g(\omega)$ . Here  $\alpha f(r(t))$  represents the adaptive coupling strength where  $\alpha$  is the nonadaptive coupling strength, i.e., when  $f(r(t)) = 1 \forall t$ . The function  $f(r(t)) > 0$  introduces the generalized-adaptive behavior into the system (see Fig. 1 for a schematic), where  $r(t)$  is the modulus of the instantaneous complex Kuramoto order parameter  $z(t)$ , given by

$$z(t) = r(t)e^{i\psi(t)} = N^{-1} \sum_{j=1}^N e^{i\phi_j(t)}, \quad (2)$$

and  $i = \sqrt{-1}$ .

It is to be noted that  $z$ ,  $r$ , and  $\psi$  are generally time-dependent, but we drop the time dependence in our notation hereafter for the sake of brevity of exposition. To analytically arrive at the synchronization transition points, the relatively simpler case of a large number of globally coupled Kuramoto oscillators is considered. This implies that  $A_{ij} = 1 - \delta_{ij}$  and  $N \rightarrow \infty$ , such that  $\langle k \rangle \approx N$ . Therefore, Eq. (1) can be

recast as

$$\frac{d\phi_i}{dt} = \omega_i + \frac{\alpha f(r)}{N} \sum_{j=1}^N \sin(\phi_j - \phi_i), \quad (3)$$

which can be further rewritten in the form

$$\dot{\phi}_i = \omega_i + \frac{\alpha f(r)}{2i} [ze^{-i\phi_i} - z^*e^{i\phi_i}], \quad (4)$$

by using the definition of  $z$  from Eq. (2). In the limit  $N \rightarrow \infty$ , the state of the system can be specified by the joint probability density function  $F(\phi, \omega; t)$ , which satisfies the continuity equation

$$\frac{\partial F}{\partial t} + \frac{\partial(F\dot{\phi})}{\partial \phi} = 0 \quad (5)$$

and

$$\int_0^{2\pi} F(\phi, \omega; t) d\phi = g(\omega). \quad (6)$$

The function  $F(\phi, \omega; t)$  can therefore be expanded as a Fourier series

$$F(\phi, \omega; t) = \frac{g(\omega)}{2\pi} \left[ 1 + \sum_{n=1}^{\infty} \tilde{F}_n(\omega, t) e^{in\phi} + \sum_{n=1}^{\infty} [\tilde{F}_n(\omega, t)]^* e^{-in\phi} \right], \quad (7)$$

where  $\tilde{F}_n(\omega, t)$  is the  $n$ th Fourier coefficient. Applying the Ott-Antonsen (OA) ansatz [50,51], the Fourier modes are assumed to be of the form

$$\tilde{F}_n(\omega, t) = [v(\omega, t)]^n, \quad (8)$$

with the restriction

$$|v(\omega, t)| < 1, \quad (9)$$

such that the infinite series in Eq. (7) converges. It is further assumed that  $|v(\omega, t)|$  can be analytically continued to the complex  $\omega$  plane, has no singularities in the lower half of the complex  $\omega$  plane, and  $|v(\omega, t)| \rightarrow 0$  for  $\text{Im}(\omega) \rightarrow -\infty$ .

Subsequently, Eq. (8), when substituted into Eq. (5) along with Eq. (4), leads to

$$\frac{\partial v(\omega, t)}{\partial t} + i\omega v(\omega, t) + \frac{\alpha f(r)}{2} [zv^2(\omega, t) - z^*] = 0. \quad (10)$$

Additionally, it follows from Eq. (2) that

$$z = \int_0^{2\pi} \int_{-\infty}^{\infty} d\phi d\omega e^{i\phi} F(\phi, \omega; t) = \int_{-\infty}^{\infty} d\omega g(\omega) v^*(\omega, t), \quad (11)$$

which simplifies to

$$z = v^*(-i\Delta, t), \quad (12)$$

if the distribution  $g(\omega)$  is assumed to be

$$g(\omega) = \frac{\Delta}{\pi} \left( \frac{1}{\omega^2 + \Delta^2} \right), \quad (13)$$

where  $\Delta$  is a constant parameter. Substituting  $\omega = -i\Delta$  into Eq. (10) and separating the real part leads to

$$\frac{dr}{dt} = G(r), \quad (14)$$

where

$$G(r) = -r \left[ \left( \Delta - \frac{\alpha f(r)}{2} \right) + \frac{\alpha f(r)r^2}{2} \right]. \quad (15)$$

Therefore, an ordinary differential equation is obtained for the order parameter  $r$  in terms of  $\alpha$ ,  $\Delta$ , and  $f(r)$ . The steady-state dynamics of  $r(t)$  can be investigated by enforcing  $\dot{r}(t) = 0$  in Eq. (14). This shows the existence of two fixed points at  $r = (0, r^*)$ . The fixed point at  $r = r^*$  is a function of  $\alpha$  and is given by the solution of the nonlinear equation

$$(r^*)^2 = 1 - \frac{2\Delta}{\alpha f(r^*)}, \quad \forall \alpha > 0. \quad (16)$$

The stability of either fixed point is determined from the behavior of the derivative of  $G(r)$  given by

$$\frac{dG}{dr} = -\Delta + \frac{\alpha f(r)}{2}[1 - 3r^2] + \frac{r\alpha f'(r)}{2}[1 - r^2], \quad (17)$$

where  $f'(r) = df/dr$ . The fixed point at  $r = 0$  is stable for values of  $\alpha$  satisfying

$$\alpha < \frac{2\Delta}{f(0)}, \quad (18)$$

whereas the fixed point  $r = r^*$  is stable for  $\forall (\alpha, r^*)$  pairs that satisfy

$$2\Delta - \alpha f(r^*) + r^* \frac{\Delta f'(r^*)}{f(r^*)} < 0. \quad (19)$$

Equation (18) and Eq. (19) suggest that there could exist a region of bistability, i.e., where both  $r = 0$  and  $r = r^*$  are simultaneously stable for some values of  $\alpha$ . In such cases, one obtains an explosive route to synchronization with two transition points: (1) at  $\alpha = \alpha_f$ , where the asynchronous state loses stability upon forward variation, and (2) at  $\alpha = \alpha_b$ , where the synchronous state loses stability upon backward variation. The forward transition point  $\alpha_f$  can be obtained from Eq. (18) and is given by

$$\alpha_f = \frac{2\Delta}{f(0)}. \quad (20)$$

From the assumption  $f(r) > 0$ , it follows that  $f(0) > 0$  which implies that  $\alpha_f$  is finite and positive. The estimation of the backward transition point  $\alpha_b$  can be posed as a minimization problem given by

$$\begin{aligned} \alpha_b = \alpha \in (0, \alpha_f] \quad & \text{minimize} \\ & \alpha \\ & \text{subject to} \\ & \times \frac{2\Delta}{f(r^*)} + r^* \frac{\Delta f'(r^*)}{[f(r^*)]^2} < \alpha. \end{aligned} \quad (21)$$

However, in the absence of such bistability, one obtains a continuous transition where the two transition points coincide at  $\alpha = \alpha_c = 2\Delta/f(0)$  where  $r^* = 0$ , and the fixed points exchange stability.

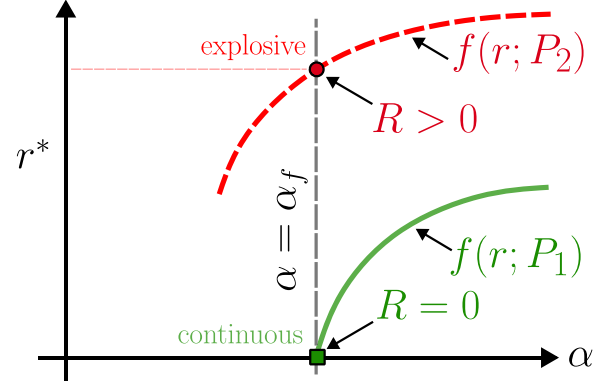


FIG. 2. Schematic of different types of transitions for  $R > 0$  (explosive) and  $R = 0$  (continuous); see Eq. (22). The curves denote the variation of  $r^*$  as a function of  $\alpha$  for two different parameter sets  $P_1$  and  $P_2$ . These are marked in green (solid line) and red (broken line) respectively.

### A. Identifying transition type

It follows from the previous discussion that, to determine the type of transition for any given  $f(\cdot)$ , it is sufficient to check the value of  $r^*$  at  $\alpha = \alpha_f$  (denoted by  $R$ ). Rewriting Eq. (16) at  $\alpha = \alpha_f$  leads to

$$R^2 = 1 - h(R), \quad (22)$$

where

$$h(R) = \frac{f(0)}{f(R)}, \quad (23)$$

the roots of which allow the determination of the transition type.

While it is straightforward to see that  $R = 0$  is always a solution of Eq. (22), it is the *only* solution if  $h(R) \geq 1$ . This is represented by the green square in Fig. 2. The nonzero solution of Eq. (22), if it exists, is always stable and greater than 0 and is represented by the red circle in Fig. 2. This case represents an explosive transition, whereas the former represents a continuous transition. Thus, the condition  $h(R) \geq 1$  allows us to distinguish between continuous and explosive transitions. The following subsections discuss the results for two different functional forms of  $f(\cdot)$ , namely, polynomial and Gaussian, and for different parameter values.

### B. Polynomial form of $f(r)$

The form of the adaptation function that has been widely reported in the literature is the power law, i.e.,  $f(r) = r^\alpha$  (for example, see [49,52–55]). It finds application in many domains such as in modeling biological oscillators [56], coupled Josephson junctions [57], and others, where the strength of the interaction increases with synchronization. Motivated by this, the functional form of  $f(r)$  is assumed to be a polynomial of the form

$$f(r) = (Ar + B)^p, \quad (24)$$

where  $A, B \in \mathbb{R}^+$  and  $p \in \mathbb{R}$  are constants. This is a more general form of the power law discussed before, and the parameters capture a variety of possible interactions which

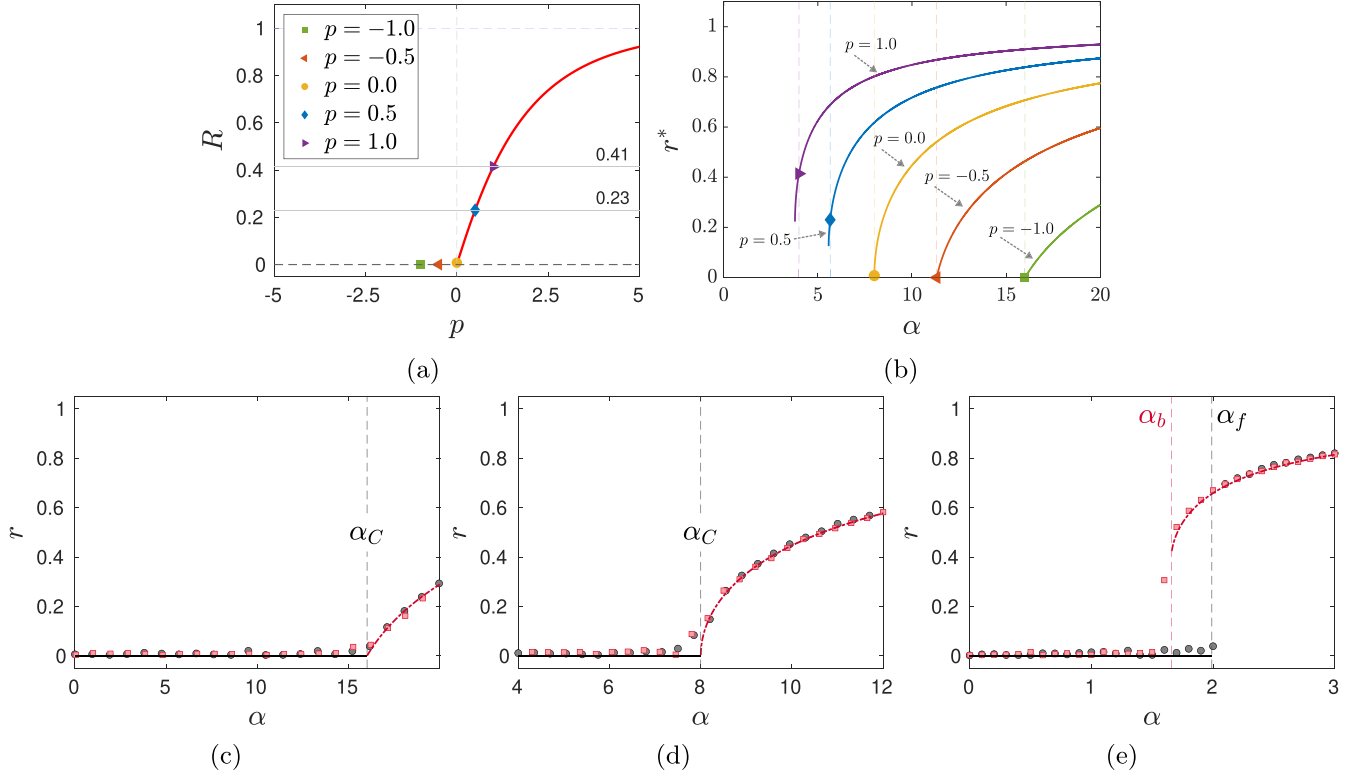


FIG. 3.  $f(r) = (Ar + B)^p$  with  $A = 1$ ,  $B = 2$ , and  $\Delta = 4$ . (a) Variation of  $R$  as a function of  $p \in [-5, 5]$  (plotted as a solid line) obtained from Eq. (22), whereas the discrete points denote values of  $R$  at specific values of  $p$ . (b) Variation of  $r^*$  as a function of  $\alpha \in [0, 20]$  for specific values of  $p$  as in (a) (plotted as solid lines), demonstrating the type of transition as  $p$  is varied. The vertical broken lines denote the corresponding values of  $\alpha_f$ , and the discrete colored points denote the value of  $R$ . (c–e) Numerically obtained variation of  $r$  (denoted by discrete points) superimposed on the analytical prediction (denoted by lines) as a function of  $\alpha$  for  $p = -1.0, 0.0$ , and  $2.0$ , respectively. The black solid line and circular markers denote the forward variation of  $\alpha$  whereas the red broken line and square markers denote the backward variation of  $\alpha$ . The vertical broken lines denote the transition point(s), i.e.,  $(\alpha_b, \alpha_f)$  or  $\alpha_C$ , depending on the type of transition.

are of different magnitudes and types (linear, quadratic, etc.), depending on the values of  $A$ ,  $B$ , and  $p$ , respectively. Additionally, for  $A = 1$ ,  $B = 0$ , Eq. (24) reduces to the previously reported form and thus captures the essential features of the results already reported in the literature.

Substituting Eq. (24) into Eq. (20), the forward transition point can be obtained as  $\alpha_f = 2\Delta B^{-p}$ . Here the expression of  $h(R)$  is obtained as

$$h(R) = \frac{1}{(1 + cR)^p}, \tag{25}$$

where  $c = A/B > 0$ . Thus, for  $p \leq 0$ ,  $h(R) \geq 1$ , which implies the transition at  $\alpha_f$  is continuous. For values of  $p > 0$ ,  $h(R) < 1$ , which implies the transition at  $\alpha_f$  is discontinuous. In Fig. 3(a) the solid red line denotes the locus of nonzero values of  $R$  obtained from Eq. (22) by varying  $p$ . Specific values of  $R$  corresponding to  $p = -1.0, -0.5, 0.0, 0.5$ , and  $1.0$  is highlighted, and the variation of  $r^*$  as a function of  $\alpha$  (obtained from Eq. (16)) corresponding to these  $p$  values is shown in Fig. 3(b). From Fig. 3(a), it is observed that for values of  $p \leq 0$ ,  $R = 0$  is the only solution, whereas for values of  $p > 0$ ,  $R > 0$  is also a solution along with  $R = 0$ . The plots in Fig. 3(b) confirm that explosive transitions are obtained for  $p > 0$  (i.e.,  $p = 0.5, 1.0$ ) and continuous transitions are obtained for  $p \leq 0$  (i.e.,  $p = -1.0, -0.5, -0.0$ ). This is further validated in Figs. 3(c), 3(d), and 3(e), which show the

numerically obtained variation of  $r$  (see Appendix A), as a function of  $\alpha$ , for  $p = -1.0, 0.0$ , and  $2.0$ . These are obtained for both forward (plotted as black circles) and backward (plotted as red squares) variations of  $\alpha$  and are superimposed on the analytical predictions, which are plotted as solid black lines and broken red lines, respectively. The plots are seen to agree remarkably well. Note that for all the results reported in this subsection and Fig. 3,  $A = 1, B = 2$ , and  $\Delta = 4$ ; see Appendix B for the corresponding plots of the adaptation functions.

### C. Gaussian form of $f(r)$

The previously chosen polynomial form, while nonlinear, is strictly monotonic in  $[0,1]$ . To incorporate nonmonotonic behavior, which is prevalent in many physical scenarios, the functional form of  $f(r)$  is assumed to be a Gaussian of the form

$$f(r) = Ae^{-B(r-C)^2}, \tag{26}$$

where  $A, B \in \mathbb{R}^+$  and  $C \in \mathbb{R}$  are constants. The Gaussian is also an appropriate approximation in many physical scenarios, especially when there are contributions from many different functional forms. Additionally, for  $A = a^2, B = 1$ , and  $C = 0$ , it reduces to the form reported recently [47].

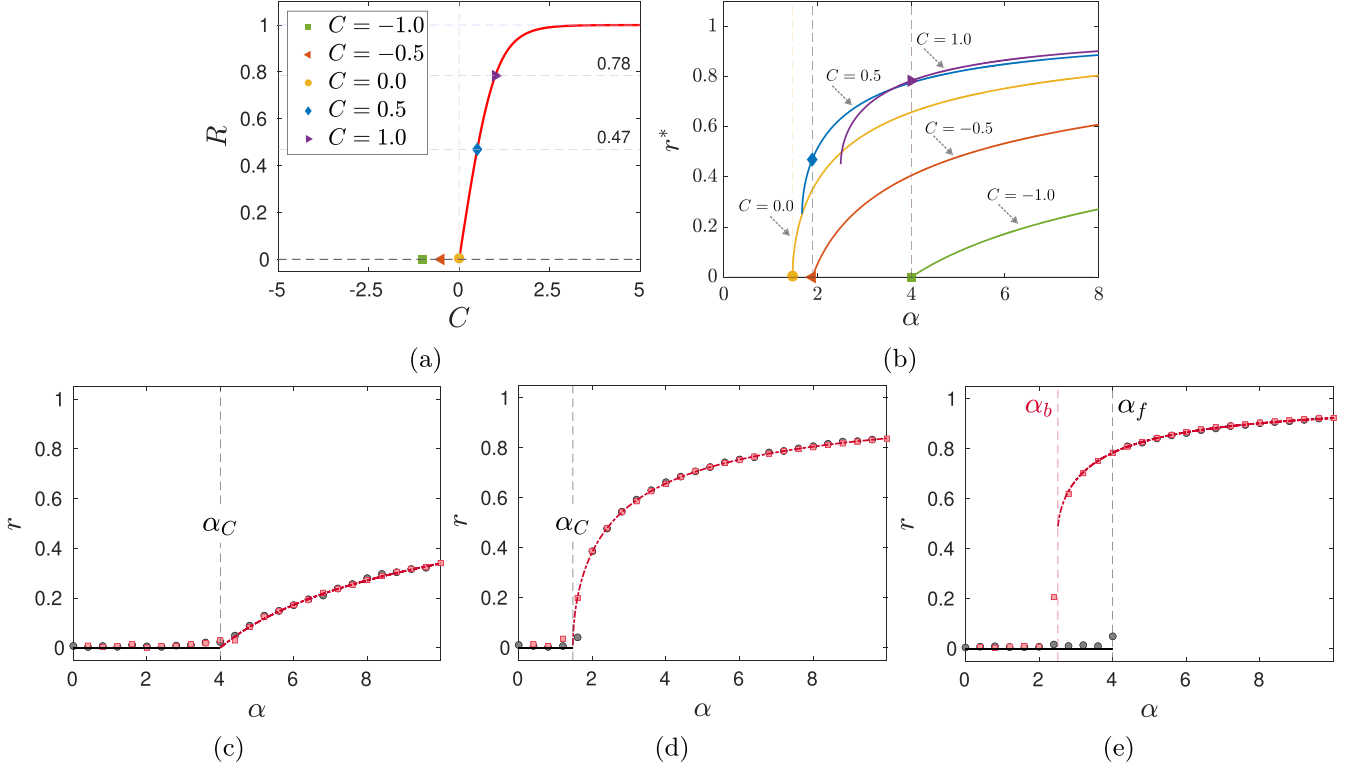


FIG. 4.  $f(r) = Ae^{-B(r-C)^2}$  with  $A = e$ ,  $B = 1$ , and  $\Delta = 2$ . (a) Variation of  $R$  as a function of  $C \in [-5, 5]$ . (b) Variation of  $r^*$  as a function of  $\alpha \in [0, 8]$  for specific values of  $C$  as in (a), demonstrating the type of transition as  $C$  is varied. (c–e) Numerically obtained variation of  $r$  superimposed on the corresponding analytical prediction as a function of  $\alpha$  for  $C = -1.0, 0.0$ , and  $1.0$  respectively. For all subfigures, the different point types, lines, and colors carry the same meaning as in Fig. 3.

Substituting Eq. (26) into Eq. (20), the forward transition point can be obtained as  $\alpha_f = 2\Delta A^{-1}e^{BC^2}$ . It is interesting to note that keeping other parameters fixed, the value  $\pm C$  results in the same value of  $\alpha_f$  due to its quadratic dependence on  $C$ . Here the expression of  $h(R)$  is obtained as

$$h(R) = e^{-2BCR\left(1 - \frac{R}{2C}\right)}. \quad (27)$$

Thus for  $C \leq 0$ ,  $h(R) \geq 1$ , implying the transition at  $\alpha_f$  is continuous. For  $C > 0$ ,  $h(R) < 1$  for  $R \in (0, 2C)$ , which implies the transition at  $\alpha_f$  is discontinuous. In Fig. 4(a), which is similar to Fig. 3(a), it is observed that  $R$  has nonzero solutions only for  $C > 0$ , implying that the transition is explosive only for such cases. This is further verified via the plot of  $r^*$  as a function  $\alpha$  for  $C = -1.0, -0.5, 0.0, 0.5$ , and  $1.0$  in Fig. 4(b). Finally, these results are numerically validated in Figs. 4(c), 4(d), and 4(e) for  $C = -1.0, 0.0$ , and  $1.0$  and are seen to agree remarkably well with the analytical predictions. The results reported in this subsection and Fig. 4 have been computed for  $A = e$ ,  $B = 1$ , and  $\Delta = 2$ ; see Appendix B for the corresponding plots of the adaptation functions.

### III. MULTILAYER CONFIGURATION

The previously introduced formalism can be generalized to the case of multilayer networks, with the interlayer coupling being adaptive (for example, see [55]). Such a system can be described by a set of  $N \times L$  coupled ODEs, analogous to

Eq. (3), of the form

$$\frac{d\phi_{i,k}}{dt} = \omega_{i,k} + \underbrace{\frac{\alpha_k f_k(\vec{r}(t))}{N} \sum_{j=1}^N \sin(\phi_{j,k} - \phi_{i,k})}_{\text{intralayer interaction}}, \quad (28)$$

adaptive interlayer interaction

where  $i = 1, 2, \dots, N$  and  $k = 1, 2, \dots, L$ ,  $N$  and  $K$  being the number of oscillators per layer and the number of layers, respectively. Here  $\vec{r} = (r_1, r_2, \dots, r_L)^T$ ,  $f_k: \mathbb{R}^L \rightarrow \mathbb{R}$  is the generalized adaptation function associated with the  $k$ th layer. Further,  $\phi_{i,k}$  and  $\omega_{i,k}$  carry the same physical connotation from Eq. (3), with the subscripts  $(i, k)$  denoting the  $i$ th oscillator from the  $k$ th layer. The synchronization order parameters of each layer  $r_k$  is defined similarly to Eq. (2), as

$$z_k = r_k e^{i\psi_k} = N^{-1} \sum_{j=1}^N e^{i\phi_{j,k}}. \quad (29)$$

It is important to note that the coupling between the layers in Eq. (28) is via the adaptation function  $\vec{f}$  and there is no explicit direct interlayer phase coupling between the oscillators across different layers, the coupling is implicitly introduced via the individual order parameters  $r_k$ . It is plausible to expect such a coupling scheme to appear in multilayer systems, especially those with *nonseparable* inter- and intralayer interactions. While most of the existing literature considers separable forms of interaction where the governing



equations can be written as a sum of inter- and intralayer interactions (for example, see [58–60]), the proposed model in Eq. (28) highlights an example of a nonseparable interaction. While such interactions could potentially be of many forms, this example combines the interlayer interaction as a generalized adaptation in the intralayer interaction term which follows as a natural extension of the adaptive coupling model discussed in Eq. (3).

Following a similar analysis as in the previous section, using the OA ansatz leads to a set of  $L$  nonlinear coupled differential equations governing the evolution of the  $L$  order parameters, given by

$$\frac{dr_k}{dt} = G_k(\vec{r}), \quad (30)$$

where

$$G_k(\vec{r}) = -r_k \left[ \left( \Delta_k - \frac{\alpha_k f_k}{2} \right) + \frac{\alpha_k f_k r_k^2}{2} \right] \quad (31)$$

and

$$\frac{\partial G_k}{\partial r_j} = \left[ -\Delta_k + \frac{\alpha_k f_k}{2} (1 - 3r_k^2) \right] \delta_{kj} + \frac{r_k \alpha_k}{2} \frac{\partial f_k}{\partial r_j} (1 - r_k^2) \quad (32)$$

denotes the corresponding Jacobian.

### Cross-adaptive coupling $\vec{f}(\vec{r})$

Among the numerous possible coupling scenarios [i.e., various forms of  $\vec{f}(\vec{r})$ ] that merit investigation, “cross”-adaptation, which is discussed next, is interesting and physically relevant. Here the intralayer coupling strength of one layer adapts to the order parameter of the other layer and vice versa (for example, see [31,55,61]) with no additional forms of interlayer interaction. This form of coupling is chosen as a simpler but physically relevant case of Eq. (28). An example of this can be the dynamics of synchronized clapping and cheering in a hotly contested sports event or political debate. In this scenario, supporters of one group would always try to be louder or turn up in larger numbers compared to their opponents (i.e., be more synchronized in their own activity). As a result, increased synchronization of one group incites the other group to be more synchronized. However, while this represents a case of positive feedback acting across the layers, there could exist other scenarios with different feedback characteristics across different layers.

The condition of cross-adaptation can be mathematically expressed by the condition

$$\frac{\partial f_k}{\partial r_k} = 0, \quad (33)$$

which implies  $f_k$  is not a function of  $r_k$ . Under this condition, the diagonal ( $j = k$ ) and off-diagonal ( $j \neq k$ ) terms of the Jacobian are, respectively, given by

$$\frac{\partial G_k}{\partial r_j} \Big|_{j=k} = -\Delta_k + \frac{\alpha_k f_k}{2} (1 - 3r_k^2) \quad (34)$$

and

$$\frac{\partial G_k}{\partial r_j} \Big|_{j \neq k} = \frac{r_k \alpha_k}{2} \frac{\partial f_k}{\partial r_j} (1 - r_k^2). \quad (35)$$

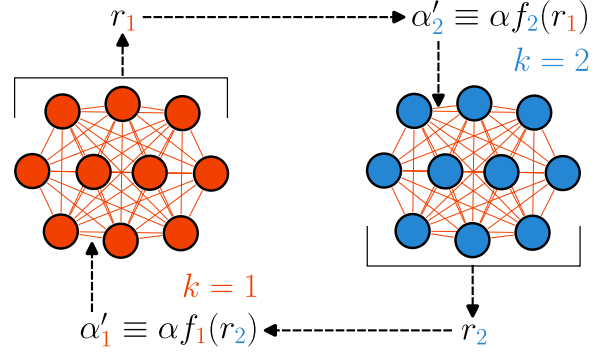


FIG. 5. Schematic of the multilayer phase oscillator system studied in Sec. III A.  $\alpha'_k$  and  $\alpha_k$  carry the same meaning as Fig. 1. Different values of  $k$  (i.e., the subscript) denote the distinct layers in the system.

It is clear from Eq. (30) that  $\vec{r} = \vec{0}$  (i.e., all layers are asynchronous) is always a solution and for which the Jacobian is diagonal. Therefore, the stability of the  $\vec{0}$  state is determined by the largest eigenvalue (i.e., the largest diagonal element) of the Jacobian and

$$\max_{k=\{1,\dots,L\}} \left[ -\Delta_k + \frac{\alpha_k f_k(\vec{0})}{2} \right] < 0 \quad (36)$$

represents the mathematical condition for stability. As an example, a bilayer system of coupled phase oscillators (see Fig. 5 for a schematic) is studied with equal intralayer coupling strength (i.e.,  $\alpha_1 = \alpha_2 = \alpha$ ) and identical natural frequency distributions (i.e.,  $\Delta_1 = \Delta_2 = \Delta$ ). For this system, the adaptation functions are defined following Eq. (33) as

$$f_k(\vec{r}) = \begin{cases} (Ar_2 + B)^p & k = 1, \\ (Ar_1 + B)^q & k = 2, \end{cases} \quad (37)$$

where  $A, B, p$ , and  $q$  are constants defined similarly to Eq. (24). Here the first layer ( $k = 1$ ) is coupled to the second layer ( $k = 2$ ) by pure adaptation and vice versa; see Appendix B. Note that our model reduces to a similar bi-layer model studied by Zhang *et al.* [55] for  $A = 1$ ,  $B = 0$ , and  $p = q = 1$ .

However, in general,  $p \neq q \neq 0$  and hence an aspect of asymmetry is introduced into the adaptive coupling between the layers. The rationale for this choice of adaptation functions is similar to that in Sec. II. The parameter values are chosen such that the two layers have very different adaptation characteristics (see Appendix B). Substituting Eq. (37) into Eq. (30) leads to

$$\frac{dr_1}{dt} = -r_1 \left[ \left( \Delta - \frac{\alpha(Ar_2 + B)^p}{2} \right) + \frac{\alpha(Ar_2 + B)^p}{2} r_1^2 \right] \quad (38)$$

and

$$\frac{dr_2}{dt} = -r_2 \left[ \left( \Delta - \frac{\alpha(Ar_1 + B)^q}{2} \right) + \frac{\alpha(Ar_1 + B)^q}{2} r_2^2 \right]. \quad (39)$$

The above are two coupled differential equations that govern the evolution of the order parameters  $r_1$  and  $r_2$  corresponding to the two layers  $k = 1$  and  $k = 2$ , respectively. The corresponding Jacobian  $J$ , essential for the linear stability analysis

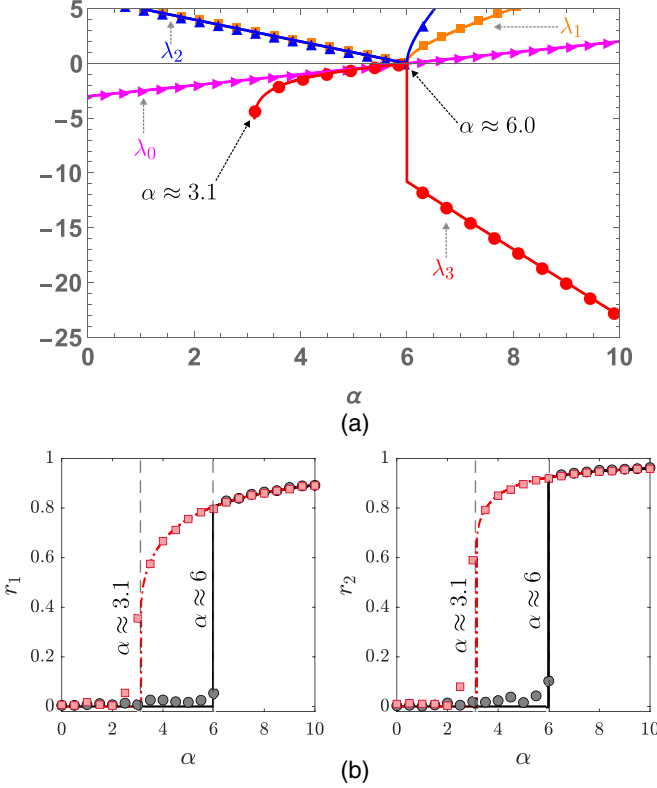


FIG. 6. Results for  $A = 2.0, B = 1.0, p = 1.0, q = 2.0$ , and  $\Delta = 3.0$ , demonstrating explosive transition. The subfigures correspond to (a) variation of  $\lambda_k$  (marked with arrows) as a function of  $\alpha \forall k$ . The different colors and line styles correspond to the different values of  $k$  and (b)  $r_1$  and  $r_2$  as a function of  $\alpha$ . Here discrete points denote values of  $r$  obtained from numerical simulation of Eq. (28), whereas the lines denote the steady-state solution of Eq. (38) and Eq. (39). The different markers, lines, and colors carry the same connotation as in Fig. 3.

of the system, is given in Appendix C. This system of equations admits four qualitatively different steady-state solutions  $(r_1^*, r_2^*)$  given by  $S_0 \equiv (0, 0)$ ,  $S_1 \equiv (0, X_2)$ ,  $S_2 \equiv (X_1, 0)$ , and  $S_3 \equiv (R_1, R_2)$ . Here

$$X_k = \sqrt{1 - \frac{2\Delta}{\alpha f_k(\bar{0})}}, \quad (40)$$

and  $\{R_1 \neq 0, R_2 \neq 0\}$  is the nonzero solution of the set of equations given by  $G_k(R_1, R_2) = 0$  for  $k = 1, 2$ . The variation of these steady states  $S_k \forall k = \{0, \dots, 3\}$ , as a function of  $\alpha$ , along with the corresponding eigenvalues of  $J$ , completely describes the synchronization characteristics in this system.

Figures 6–9 show the results for the four different parameter sets that demonstrate qualitatively different synchronization phenomena occurring in the system governed by Eq. (28) and Eq. (37).

Subfigure (a) of each of these figures show the variation of the largest eigenvalue of  $J$ , denoted by  $\lambda_k$  and marked with an arrow, computed for each steady state  $S_k$ , as a function of  $\alpha$ . The different line markers and colors correspond to different values of  $k$ . Here (a) the magenta line with right triangle markers corresponds to  $k = 0$ , (b) the yellow line with

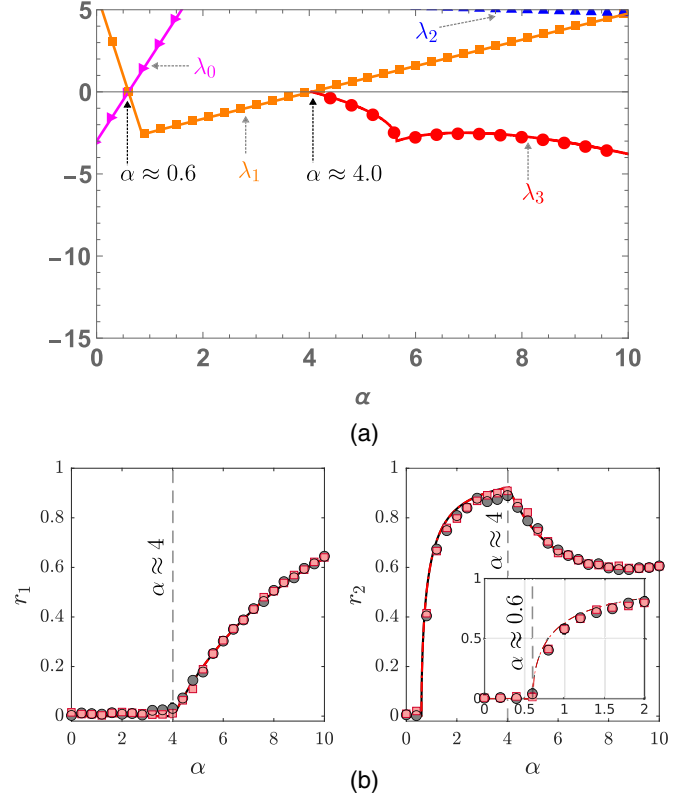


FIG. 7. Results for  $A = 1.5, B = 0.1, p = 1.0, q = -1.0$ , and  $\Delta = 3.0$ , demonstrating continuous transition. The subfigures and the different plot styles have identical implications as in Fig. 6.

square markers corresponds to  $k = 1$ , (c) the blue line with upward triangle markers corresponds to  $k = 2$ , and (d) the red line with circular markers corresponds to  $k = 3$ . Subfigure (b) of these figures shows the variation with  $\alpha$  of the order parameters  $r_1$  and  $r_2$  computed numerically by solving Eq. (28) (plotted as discrete points), along with the steady-state solution of Eq. (38) and Eq. (39) (plotted as lines). Here (1) the black solid line and circular markers denote the forward variation of  $\alpha$ , whereas (2) the red broken line and square markers denote the backward variation of  $\alpha$ . Specifically, Figs. 6 and 7 demonstrate the two commonly observed synchronization transitions, i.e., explosive and continuous. Figures 8 and 9 demonstrate two slightly different cases, denoted here as Type 1 and Type 2, (also see [62]) of what is called “tiered” transition [63]. Both continuous and explosive transitions are encountered en route to synchronization and the difference between them is highlighted during desynchronization. The following subsections discuss these in more detail.

### 1. Explosive and continuous transitions

In Fig. 6(a) it is seen that the eigenvalues  $\lambda_0$  and  $\lambda_3$  are negative for  $\alpha \in [3.1, 6]$ , which indicates the states  $S_0$  and  $S_3$  are simultaneously stable in that range. As discussed earlier, this induces explosive transition at the boundaries of this region as  $\alpha$  is varied across this range. Thus, upon forward variation of  $\alpha$ , the system explosively transitions from  $S_0$  to  $S_3$  at  $\alpha = 6$ , and upon backward variation of  $\alpha$ , the system explosively transitions from  $S_3$  to  $S_0$  at  $\alpha \approx 3.1$ . However, for

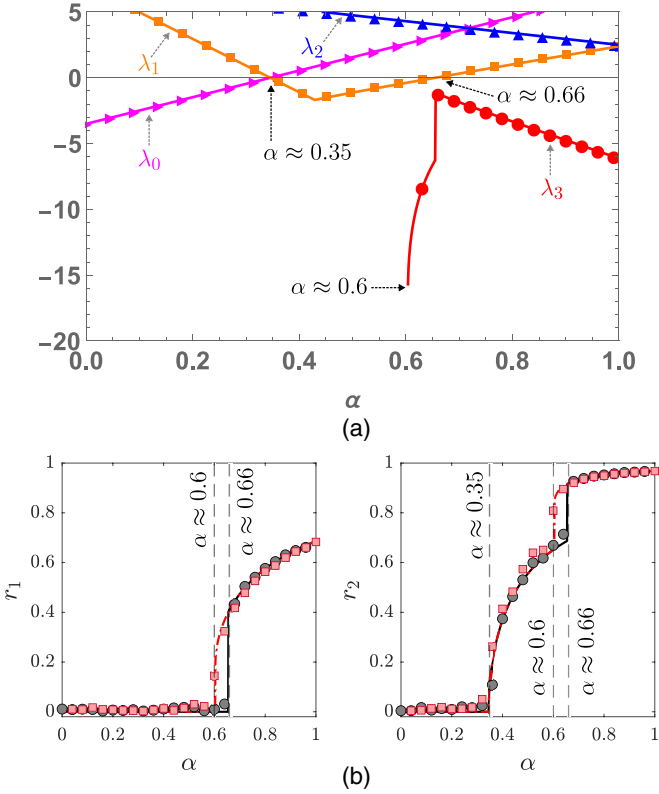


FIG. 8. Results for  $A = 9.0, B = 4.5, p = 1.0, q = 2.0,$  and  $\Delta = 3.5$ , demonstrating type 1 tiered transition. The subfigures and the different plot styles have identical implications as in Fig. 6.

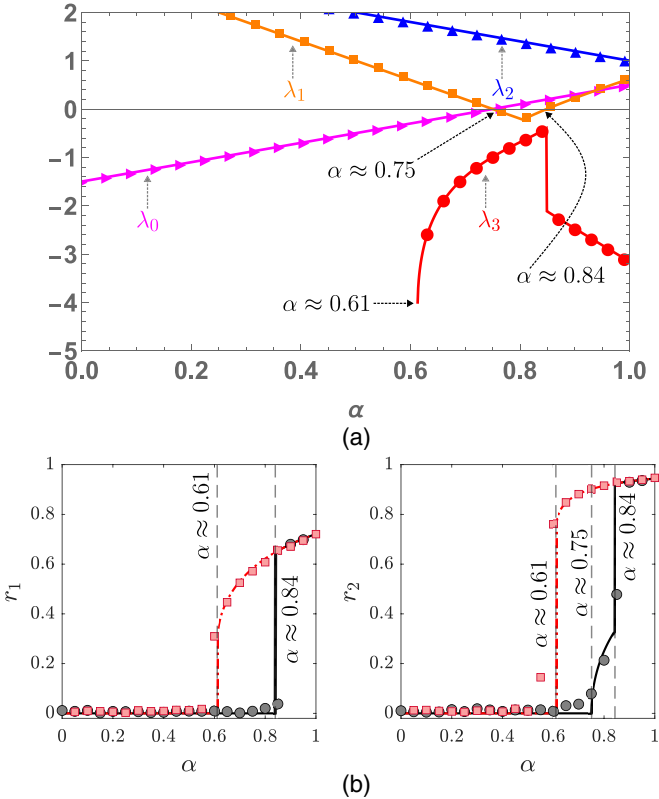


FIG. 9. Results for  $A = 4.5, B = 2.0, p = 1.0, q = 2.0,$  and  $\Delta = 1.5$ , demonstrating type 2 tiered transition. The subfigures and the different plot styles have identical implications as in Fig. 6.

$\alpha < 3.1$  and  $\alpha > 6$ ,  $\lambda_0$  and  $\lambda_3$  are the sole negative eigenvalues respectively. This implies that the system is monostable in these regions with the states  $S_0$  and  $S_3$  respectively. These transition points and the variation of the steady-state order parameters are numerically validated in Fig. 6(b).

In Fig. 7(a) it is seen that no two eigenvalues are simultaneously negative for any value of  $\alpha$ . However, at least one eigenvalue is always negative for the entire region. Specifically, for  $\alpha < 0.6$ ,  $\alpha \in [0.6, 4.0]$ , and  $\alpha > 4.0$ , the negative eigenvalues are  $\lambda_0$ ,  $\lambda_1$  and  $\lambda_3$  respectively. This implies that the stability regions of the different states are nonoverlapping, i.e., the states are monostable. As discussed earlier, this implies that the transitions are continuous at the stability boundaries of each steady state. Thus, upon forward variation of  $\alpha$ , the system undergoes a continuous transition from  $S_0$  to  $S_1$  at  $\alpha \approx 0.6$ . Upon further increasing  $\alpha$ , the system undergoes another continuous transition from  $S_1$  to  $S_3$  at  $\alpha \approx 4$ . Curiously, for  $\alpha > 4$ , in contrast to  $r^{(1)}$  which increases monotonically, there is a decrease in  $r^{(2)}$ , due to this particular choice of the parameters. Since all the transitions are continuous, the backward variation of  $\alpha$  leads to the same set of transitions but in reverse sequence. Figure 7(b) provides the numerical validation of these transition points and the variation of the steady-state order parameters.

### 2. Tiered transitions

In Fig. 8(a) the variation of  $\lambda_k$ , as a function of  $\alpha$ , can be divided into four distinct regimes: (1)  $\alpha < 0.35$ , where only  $\lambda_0$  is negative; (2)  $\alpha \in [0.35, 0.66]$ , where only  $\lambda_1$  is negative; (3)  $\alpha \in [0.66, 0.66]$ , where both  $\lambda_1$  and  $\lambda_3$  are negative; and (4)  $\alpha > 0.66$ , where only  $\lambda_3$  is negative. Thus, for the first two regimes,  $S_0$  and  $S_1$  are the only stable states respectively. For the third regime,  $S_1$  and  $S_3$  are simultaneously stable, whereas for the fourth regime,  $S_3$  is the sole stable state. Thus, upon forward variation of  $\alpha$ , the system undergoes a continuous transition from  $S_0$  to  $S_1$  at  $\alpha \approx 0.35$ . Upon further increasing  $\alpha$  adiabatically, the system remains in  $S_1$  till  $\alpha < 0.66$ , and then undergoes an explosive transition from  $S_1$  to  $S_3$  at  $\alpha \approx 0.66$  since  $S_1$  loses stability. This results in a highly synchronous state. Upon backward variation of  $\alpha$ , the system continues to remain in  $S_3$  upon crossing the right bistable boundary at  $\alpha = 0.66$ . However, at  $\alpha = 0.6$ , i.e., the left boundary of the bistability regime,  $S_3$  loses stability and the system transitions from  $S_3$  to  $S_1$  explosively. Further decreasing  $\alpha$  leads to a continuous transition from  $S_1$  to  $S_0$  at  $\alpha \approx 0.35$ , coinciding with the forward transition point, resulting in a completely asynchronous state. The numerical verification of these transition points and the corresponding variation of the steady-state order parameters is presented in Fig. 8(b).

For the case presented in Fig. 9(a), the variation of  $\lambda_k$ , as a function of  $\alpha$ , can also be divided into four distinct regions: (1)  $\alpha < 0.61$ , where only  $\lambda_0$  is negative; (2)  $\alpha \in [0.61, 0.75]$ , where both  $\lambda_0$  and  $\lambda_3$  are negative; (3)  $\alpha \in [0.75, 0.84]$ , where both  $\lambda_1$  and  $\lambda_3$  are negative; and (4)  $\alpha > 0.84$ , where only  $\lambda_3$  is negative. Thus, for the first region, only  $S_0$  is stable. The following two regions are bistable with  $S_0, S_3$  and  $S_1, S_3$  being the respective stable states. Finally, in the fourth region,  $S_3$  is the only stable state. Thus, upon forward variation of  $\alpha$ , the system remains in  $S_0$  till  $\alpha < 0.75$ . At  $\alpha \approx 0.75$ , the



systems switches to the nearest stable state  $S_1$  and continues till  $\alpha < 0.84$ . At  $\alpha \approx 0.84$ ,  $S_1$  loses stability and the system explosively transitions to  $S_3$  resulting in a highly synchronous state. Upon backward variation of  $\alpha$ , the system remains in  $S_3$  across the right bistable boundary and only undergoes an explosive transition from  $S_3$  to  $S_0$  directly at  $\alpha \approx 0.61$  where  $S_3$  loses stability, thereby resulting in a completely asynchronous state. This is in contrast to the previous case where the desynchronization involves both explosive and continuous transitions. Figure 9(b) illustrates the numerical validation of these transition points, along with the variation in steady-state order parameters.

#### IV. CONCLUSIONS

This study investigates the various routes to synchrony in globally coupled Kuramoto oscillators with pairwise interactions, such that the strength of the coupling adapts according to the global dynamics, which is quantified through the instantaneous value of the order parameter  $r(t)$ . The exact relationship between the coupling strength and the order parameter is dictated by the physical scenario under consideration and is modeled through a nonlinear function  $f(\cdot)$ . Analytical developments presented in this study, based on the Ott-Antonsen, enable inferring the type of transition from the form of  $f(x)$  via a simple algebraic equation, the roots of which dictate the type of transition. The developments are applicable for a wide class of functional forms of  $f(\cdot)$ , satisfying certain criteria. The validity of these results is demonstrated for two broad classes of  $f(\cdot)$ : (1) polynomial, which is monotonic and (2) Gaussian, which is nonmonotonic. These are chosen for their generality, wide applicability, and are shown to induce different synchronization transitions.

These developments are subsequently generalized to multilayer networks where the coupling strength of each layer depends on the order parameters associated with each of the other layers. It is shown that the routes to synchrony are completely characterized through the largest eigenvalue of the Jacobian corresponding to the reduced system obtained via the Ott-Antonsen ansatz. The results are demonstrated through a bilayer network with cross-adaptation. This system exhibits rich dynamical behavior and a multitude of routes to synchrony depending on the monotonicity and relative magnitudes of the adaptation functions. Specifically, certain parameter values are seen to induce tiered synchronization transitions in addition to explosive and continuous transitions. The analytical developments presented are shown to exactly capture all these intricate complexities of the various transition scenarios and contribute to a better understanding of real-life complex systems. Further studies are ongoing with applications of generalized adaptive dynamics to systems with complex intra- and interlayer topologies, which can potentially show even richer dynamical phenomena.

The computer programs and the generated data used in this study are available from the corresponding author upon reasonable request.

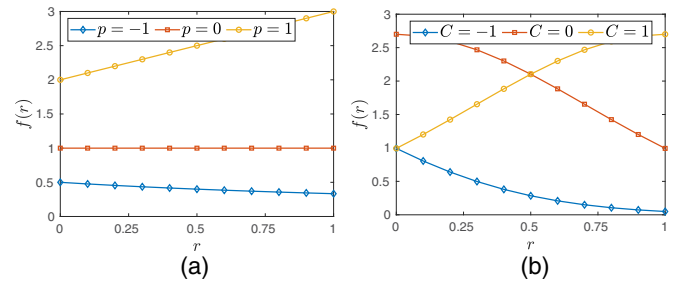


FIG. 10. Plot of the adaptation functions used in (a) Fig. 3 where  $f(r) = (Ar + B)^p$  for  $A = 1.0$ ,  $B = 2.0$  and (b) Fig. 4 where  $f(r) = Ae^{-B(r-C)^2}$  for  $A = e$ ,  $B = 1.0$ .

#### ACKNOWLEDGMENTS

The authors would like to acknowledge the funding received from the Ministry of Education, Government of India towards the Center for Complex Systems and Dynamics, IIT Madras (Project No. SP2021077 DRMHRD/DIRIIT).

#### APPENDIX A: SIMULATION DETAILS

For numerical simulations of Eq. (3), Eq. (28), and the evaluation of the order parameter(s),  $N$  is taken to be  $2.5 \times 10^4$ . The dynamical equations were integrated by the classic fourth-order Runge-Kutta method on an NVIDIA GPU using code written in C++ and OpenACC. The time step  $\delta t$  was taken to be  $10^{-4}$  and the simulations were run for at least  $10^5$  steps. The forward and backward variation of the order parameter(s) as a function of  $\alpha$  (i.e., the discrete data points in black and red respectively in the synchronization transition diagrams) was obtained by using the final state of the system for the current value of  $\alpha$  as the initial condition of the system for next value of  $\alpha \rightarrow \alpha \pm \delta\alpha$ . The value of  $\delta\alpha$  was appropriately chosen such that the transitions are well captured.

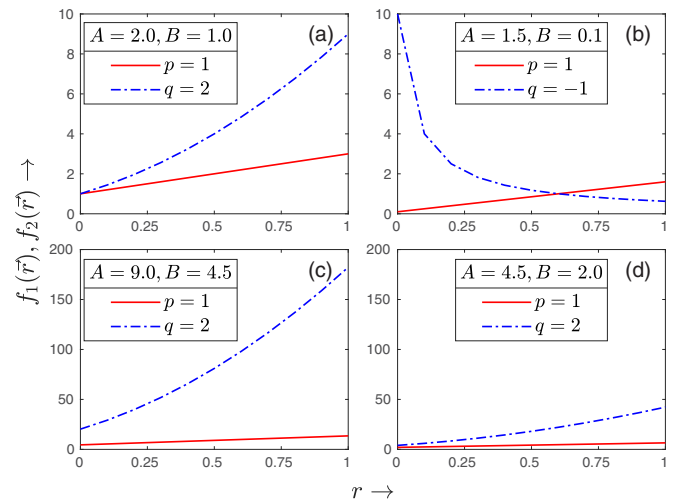


FIG. 11. Plot of the adaptation functions (i.e.,  $f_k$  as a function of  $r$ ) used in Figs. 6–9 [here (a), (b), (c), and (d), respectively]; see Eq. (37). The red (solid line) and blue (broken line) lines correspond to  $f_1$  and  $f_2$ , respectively. These figures highlight the contrasting adaptation characteristics in the two layers.

## APPENDIX B: ADAPTATION FUNCTIONS USED IN SEC. II AND SEC. III A

Figures 10 and 11 show the plots of the various different adaptation functions used in the simulations reported in Sec. II and Sec. III A, for  $r \in [0, 1]$ . Specifically, Fig. 11 showcases the contrasting adaptation characteristics of the different layers in the bilayer model discussed in Sec. III A. Figure 11(a) showcases a scenario where the adaptation functions are similar (i.e., strictly monotonic) and of similar magnitude, whereas Fig. 11(b) showcases a scenario where the adaptation function is strictly monotonically increasing on one layer and strictly monotonically decreasing on the other. Figures 11(c) and 11(d) showcase two scenarios where the adaptation functions are similar (i.e., strictly monotonically increasing) but the magnitudes are widely different on different layers.

## APPENDIX C: JACOBIAN FOR EQ. (38) AND EQ. (39)

The elements  $J_{ij}$  of the  $2 \times 2$  Jacobian  $J$  for Eq. (38) and Eq. (39) are given by

$$J_{11} = -\frac{1}{2}\alpha(3x^2 - 1)(Ay + B)^p - \Delta, \quad (\text{C1a})$$

$$J_{12} = -\frac{1}{2}\alpha A p x(x^2 - 1)(Ay + B)^{p-1}, \quad (\text{C1b})$$

$$J_{21} = -\frac{1}{2}\alpha A q y(y^2 - 1)(Ax + B)^{q-1}, \quad (\text{C1c})$$

$$J_{22} = -\frac{1}{2}\alpha(3y^2 - 1)(Ax + B)^q - \Delta, \quad (\text{C1d})$$

where  $r_1 \equiv x$  and  $r_2 \equiv y$  for the sake of brevity.

- 
- [1] S. Boccaletti, J. Kurths, G. Osipov, D. Valladares, and C. Zhou, The synchronization of chaotic systems, *Phys. Rep.* **366**, 1 (2002).
- [2] A. Pikovsky, M. Rosenblum, and J. Kurths, *Synchronization: A Universal Concept in Nonlinear Sciences*, 1st ed. (Cambridge University Press, Cambridge, 2003).
- [3] S. Chishti and R. Ramaswamy, Design strategies for generalized synchronization, *Phys. Rev. E* **98**, 032217 (2018).
- [4] I. Belykh, E. de Lange, and M. Hasler, Synchronization of bursting neurons: What matters in the network topology, *Phys. Rev. Lett.* **94**, 188101 (2005).
- [5] Y. Penn, M. Segal, and E. Moses, Network synchronization in hippocampal neurons, *Proc. Natl. Acad. Sci. USA* **113**, 3341 (2016).
- [6] B. B. Johnson, S. V. Dhople, A. O. Hamadeh, and P. T. Krein, Synchronization of nonlinear oscillators in an Iti electrical power network, *IEEE Trans. Circuit Syst. I* **61**, 834 (2014).
- [7] R. Yamapi and P. Wofo, Dynamics and synchronization of coupled self-sustained electromechanical devices, *J. Sound Vib.* **285**, 1151 (2005).
- [8] D. Pu, X. Wei, L. Xu, Z. Jiang, and R. Huan, Synchronization of electrically coupled micromechanical oscillators with a frequency ratio of 3:1, *Appl. Phys. Lett.* **112**, 013503 (2018).
- [9] S. Vishal, A. Raaj, C. Bose, and J. Venkatramani, Routes to synchronization in a pitch-plunge aeroelastic system with coupled structural and aerodynamic nonlinearities, *Int. J. Non-Linear Mech.* **135**, 103766 (2021).
- [10] A. Raaj, J. Venkatramani, and S. Mondal, Synchronization of pitch and plunge motions during intermittency route to aeroelastic flutter, *Chaos* **29**, 043129 (2019).
- [11] D. Tripathi, R. Shreenivas, C. Bose, S. Mondal, and J. Venkatramani, Experimental investigation on the synchronization characteristics of a pitch-plunge aeroelastic system exhibiting stall flutter, *Chaos* **32**, 073114 (2022).
- [12] J. Li, Z.-H. Zhou, S. Wan, Y.-L. Zhang, Z. Shen, M. Li, C.-L. Zou, G.-C. Guo, and C.-H. Dong, All-optical synchronization of remote optomechanical systems, *Phys. Rev. Lett.* **129**, 063605 (2022).
- [13] J.-P. Goedgebuer, L. Larger, and H. Porte, Optical cryptosystem based on synchronization of hyperchaos generated by a delayed feedback tunable laser diode, *Phys. Rev. Lett.* **80**, 2249 (1998).
- [14] J. M. González-Miranda, *Synchronization and Control of Chaos: An Introduction for Scientists and Engineers* (World Scientific, 2004).
- [15] F. Dörfler, M. Chertkov, and F. Bullo, Synchronization in complex oscillator networks and smart grids, *Proc. Natl. Acad. Sci. USA* **110**, 2005 (2013).
- [16] J. A. Acebrón, L. L. Bonilla, C. J. Pérez Vicente, F. Ritort, and R. Spigler, The Kuramoto model: A simple paradigm for synchronization phenomena, *Rev. Mod. Phys.* **77**, 137 (2005).
- [17] F. A. Rodrigues, T. K. D. Peron, P. Ji, and J. Kurths, The Kuramoto model in complex networks, *Phys. Rep.* **610**, 1 (2016).
- [18] D. Cumin and C. Unsworth, Generalising the Kuramoto model for the study of neuronal synchronisation in the brain, *Physica D* **226**, 181 (2007).
- [19] R. Schmidt, K. J. LaFleur, M. A. de Reus, L. H. van den Berg, and M. P. van den Heuvel, Kuramoto model simulation of neural hubs and dynamic synchrony in the human cerebral connectome, *BMC Neurosci.* **16**, 1 (2015).
- [20] A. Mohseni, S. Gharibzadeh, and F. Bakouie, The role of driver nodes in managing epileptic seizures: Application of Kuramoto model, *J. Theor. Biol.* **419**, 108 (2017).
- [21] G. Filatella, A. H. Nielsen, and N. F. Pedersen, Analysis of a power grid using a Kuramoto-like model, *Eur. Phys. J. B* **61**, 485 (2008).
- [22] F. Dörfler and F. Bullo, Synchronization and transient stability in power networks and nonuniform Kuramoto oscillators, *SIAM J. Control Optim.* **50**, 1616 (2012).
- [23] Y.-P. Choi and Z. Li, Synchronization of nonuniform Kuramoto oscillators for power grids with general connectivity and dampings, *Nonlinearity* **32**, 559 (2019).
- [24] V. Fioriti, S. Ruzzante, E. Castorini, E. Marchei, and V. Rosato, Stability of a distributed generation network using the Kuramoto models, in *International Workshop on Critical Information Infrastructures Security*, edited by R. Setola and S. Geretshuber (Springer, Berlin, Heidelberg, 2009), pp. 14–23.
- [25] Y. Ikeda, H. Aoyama, Y. Fujiwara, H. Iyetomi, K. Ogimoto, W. Souma, and H. Yoshikawa, Coupled oscillator model of the business cycle with fluctuating goods markets, *Prog. Theor. Phys. Suppl.* **194**, 111 (2012).
- [26] A. Savostianov, A. Shapoval, and M. Shnirman, Dynamics of phase synchronization between solar polar magnetic fields

- assessed with Van der Pol and Kuramoto models, *Entropy* **22**, 945 (2020).
- [27] A. Pluchino, V. Latora, and A. Rapisarda, Compromise and synchronization in opinion dynamics, *Eur. Phys. J. B* **50**, 169 (2006).
- [28] E. Blanter, J.-L. Le Mouél, M. Shnirman, and V. Courtillot, Kuramoto model with non-symmetric coupling reconstructs variations of the solar-cycle period, *Sol. Phys.* **291**, 1003 (2016).
- [29] S. Pranesh and S. Gupta, Explosive death transitions in complex networks of limit cycle and chaotic systems, *Chaos Solit. Fractals* **168**, 113112 (2023).
- [30] D. Biswas and S. Gupta, Ageing transitions in a network of rulkov neurons, *Sci. Rep.* **12**, 1 (2022).
- [31] P. Khanra, P. Kundu, C. Hens, and P. Pal, Explosive synchronization in phase-frustrated multiplex networks, *Phys. Rev. E* **98**, 052315 (2018).
- [32] A. D. Kachhvah and S. Jalan, Multiplexing induced explosive synchronization in Kuramoto oscillators with inertia, *Europhys. Lett.* **119**, 60005 (2017).
- [33] M. Kumar and S. Gupta, Route to synchronization in coupled phase oscillators with frequency-dependent coupling: Explosive or continuous? *Phys. Rev. E* **106**, 044310 (2022).
- [34] A. D. Kachhvah and S. Jalan, Delay regulated explosive synchronization in multiplex networks, *New J. Phys.* **21**, 015006 (2019).
- [35] X. Wang, Z. Zheng, and C. Xu, Explosive synchronization in phase oscillator populations with attractive and repulsive adaptive interactions, *Chaos Solit. Fractals* **170**, 113351 (2023).
- [36] J. Chen, J. Cao, and W. Huang, Traffic-driven explosive synchronization with adaptive local routing in complex networks, *Chaos Solit. Fractals* **168**, 113142 (2023).
- [37] A. P. Millán, J. J. Torres, and G. Bianconi, Explosive higher-order Kuramoto dynamics on simplicial complexes, *Phys. Rev. Lett.* **124**, 218301 (2020).
- [38] G. Ramesan, E. Shajan, and M. D. Shrimali, Explosive synchronization induced by environmental coupling, *Phys. Lett. A* **441**, 128147 (2022).
- [39] D. Biswas and S. Gupta, Mirroring of synchronization in a bi-layer master-slave configuration of Kuramoto oscillators, *Chaos* **32**, 093148 (2022).
- [40] N. Frolov, V. Maksimenko, S. Majhi, S. Rakshit, D. Ghosh, and A. Hramov, Chimera-like behavior in a heterogeneous Kuramoto model: The interplay between attractive and repulsive coupling, *Chaos* **30**, 081102 (2020).
- [41] J. Fialkowski, S. Yanchuk, I. M. Sokolov, E. Schöll, G. A. Gottwald, and R. Berner, Heterogeneous nucleation in finite-size adaptive dynamical networks, *Phys. Rev. Lett.* **130**, 067402 (2023).
- [42] R. Gutiérrez, A. Amann, S. Assenza, J. Gómez-Gardeñes, V. Latora, and S. Boccaletti, Emerging meso- and macroscales from synchronization of adaptive networks, *Phys. Rev. Lett.* **107**, 234103 (2011).
- [43] R. Berner, J. Sawicki, and E. Schöll, Birth and stabilization of phase clusters by multiplexing of adaptive networks, *Phys. Rev. Lett.* **124**, 088301 (2020).
- [44] V. Avalos-Gaytán, J. A. Almendral, I. Leyva, F. Battiston, V. Nicosia, V. Latora, and S. Boccaletti, Emergent explosive synchronization in adaptive complex networks, *Phys. Rev. E* **97**, 042301 (2018).
- [45] C. H. Waddington, Evolutionary adaptation, *Perspect. Biol. Med.* **2**, 379 (1959).
- [46] R. Thornhill, The study of adaptation, in *Interpretation and Explanation in the Study of Animal Behavior*, edited by M. Bekoff and D. Jamieson (Routledge, New York, 2021), pp. 31–62.
- [47] X. Jin, Y.-G. Wu, H.-P. Lü, and C. Xu, Synchronization dynamics of phase oscillators with generic adaptive coupling, *Commun. Theor. Phys.* **75**, 045601 (2023).
- [48] C. Xu, X. Wang, Z. Zheng, and Z. Cai, Stability and bifurcation of collective dynamics in phase oscillator populations with general coupling, *Phys. Rev. E* **103**, 032307 (2021).
- [49] G. Filatrella, N. F. Pedersen, and K. Wiesenfeld, Generalized coupling in the Kuramoto model, *Phys. Rev. E* **75**, 017201 (2007).
- [50] E. Ott and T. M. Antonsen, Low dimensional behavior of large systems of globally coupled oscillators, *Chaos* **18**, 037113 (2008).
- [51] E. Ott and T. M. Antonsen, Long time evolution of phase oscillator systems, *Chaos* **19**, 023117 (2009).
- [52] Z. Cai, Z. Zheng, and C. Xu, Exact dynamics of phase transitions in oscillator populations with nonlinear coupling, *Commun. Nonlinear Sci. Numer. Simul.* **107**, 106129 (2022).
- [53] W. Zou and J. Wang, Dynamics of the generalized Kuramoto model with nonlinear coupling: Bifurcation and stability, *Phys. Rev. E* **102**, 012219 (2020).
- [54] P. Rajwani, A. Suman, and S. Jalan, Tiered synchronization in Kuramoto oscillators with adaptive higher-order interactions, *Chaos* **33**, 061102 (2023).
- [55] X. Zhang, S. Boccaletti, S. Guan, and Z. Liu, Explosive synchronization in adaptive and multilayer networks, *Phys. Rev. Lett.* **114**, 038701 (2015).
- [56] F. Giannuzzi, D. Marinazzo, G. Nardulli, M. Pellicoro, and S. Stramaglia, Phase diagram of a generalized Winfree model, *Phys. Rev. E* **75**, 051104 (2007).
- [57] G. Filatrella, N. F. Pedersen, and K. Wiesenfeld, Synchronization of Josephson vortices in multi-junction systems, *Physica C* **437–438**, 65 (2006).
- [58] A. Kumar, S. Jalan, and A. D. Kachhvah, Interlayer adaptation-induced explosive synchronization in multiplex networks, *Phys. Rev. Res.* **2**, 023259 (2020).
- [59] S. Jalan, A. D. Kachhvah, and H. Jeong, Explosive synchronization in multilayer dynamically dissimilar networks, *J. Comput. Sci.* **46**, 101177 (2020).
- [60] P. B. Jain, T. T. Nguyen, J. Mináč, L. E. Muller, and R. C. Budzinski, Composed solutions of synchronized patterns in multiplex networks of Kuramoto oscillators, *Chaos* **33**, 103128 (2023).
- [61] P. Khanra and P. Pal, Explosive synchronization in multilayer networks through partial adaptation, *Chaos Solitons Fractals* **143**, 110621 (2021).
- [62] M. Manoranjani, D. Senthikumar, and V. Chandrasekar, Diverse phase transitions in Kuramoto model with adaptive mean-field coupling breaking the rotational symmetry, *Chaos Solitons Fractals* **175**, 113981 (2023).
- [63] P. S. Skardal and C. Xu, Tiered synchronization in coupled oscillator populations with interaction delays and higher-order interactions, *Chaos* **32**, 053120 (2022).